

# Nonlinear Isometric Manifold Learning for Injective Normalizing Flows

Eike Cramer<sup>a,b</sup>, Felix Rauh<sup>a,b</sup>, Alexander Mitsos<sup>c,a,d</sup>, Raúl Tempone<sup>e,f</sup>, Manuel Dahmen<sup>a,\*</sup>

<sup>a</sup> Forschungszentrum Jülich GmbH, Institute of Energy and Climate Research, Energy Systems Engineering (IEK-10), Jülich 52425, Germany

<sup>b</sup> RWTH Aachen University Aachen 52062, Germany

<sup>c</sup> JARA-ENERGY, Jülich 52425, Germany

<sup>d</sup> RWTH Aachen University, Process Systems Engineering (AVT.SVT), Aachen 52074, Germany

<sup>e</sup> RWTH Aachen University, Chair of Mathematics for Uncertainty Quantification, Aachen 52062, Germany

<sup>f</sup> King Abdullah University of Science and Technology (KAUST), Computer, Electrical, and Mathematical Sciences & Engineering Division (CEMSE), Saudi Arabia

To model manifold data using normalizing flows, we propose to employ the isometric autoencoder to design nonlinear encodings with explicit inverses. The isometry allows us to separate manifold learning and density estimation and train both parts to high accuracy. Applied to the MNIST data set, the combined approach generates high-quality images.

## 1 Introduction

Deep generative models (DGMs), i.e., deep learning-based probability distribution models for high-dimensional and nontrivial data [1], have gained increasing attention in many scientific fields. The two most prominent DGMs, namely, variational autoencoders (VAEs) [2] and generative adversarial networks (GANs) [3], both learn implicit representations of the probability distributions, i.e., GANs and VAEs sample data without describing the probability density functions (PDFs) directly [1]. The lack of PDFs implies that VAEs and GANs cannot be trained via likelihood maximization and, instead, must rely on approximate and adversarial training algorithms, respectively. These training algorithms are often unstable and do not necessarily converge to the true distribution [4, 1]. A third type of DGMs, the normalizing flow, models the probability distribution as a bijective transformation of a Gaussian. Using the inverse of this transformation, normalizing flows can compute the PDF explicitly, which enables training via the statistically consistent and asymptotically efficient [5] likelihood maximization [6, 7].

Despite the advantage of likelihood maximization, normalizing flows often result in poor fits of the target probability distributions [8, 9]. For instance, our previous work [10] has shown that the application of a standard normalizing flow model to energy time series data results in the sampling of uncharacteristically noisy data. The poor fits are a direct result of the structural setup of the normalizing flow that is ill-posed to describe probability distributions over lower-dimensional mani-

folds [8, 9]. As the probability distributions of many high-dimensional data sets reside on lower-dimensional manifolds [11, 12], the inability of normalizing flows to fit such probability distributions rescinds the advantages gained from the direct likelihood maximization.

In Cramer et al. [10], we have addressed the manifold structure of renewable energy time series data via dimensionality reduction using the principal component analysis (PCA), which transforms the data into a latent space without a manifold structure. Our theoretical analysis highlighted that the PDF described by the normalizing flow is invariant to the PCA. In numerical experiments, we showed that PCA works well for the considered time series data sets, and we were able to sample realistic scenarios of photovoltaic and wind power generation as well as load demand data. However, the affine PCA fails to encode data sets that reside on nonlinear manifolds. In this work, we build on our findings on the PCA dimensionality reduction to generalize our approach to nonlinear encodings, in particular, isometric nonlinear encodings.

Alternative approaches to training normalizing flows on manifold data also set up the normalizing flow with a lower-dimensional latent space, i.e., they match the manifold data with a lower-dimensional Gaussian [13, 8]. To this end, the bijective transformation is substituted with an injective transformation, i.e., a pseudo invertible transformation that maps the data to a lower-dimensional space [13]. Such injective normalizing flows then combine manifold learning with density estimation in a single model and, thus, a simultaneous training approach.

\*Manuel Dahmen, Forschungszentrum Jülich GmbH, Institute of Energy and Climate Research, Energy Systems Engineering (IEK-10), Jülich 52425, Germany  
E-mail: m.dahmen@fz-juelich.de

Some of the published approaches assume a dimensionality reducing map to be known and available a priori [13, 14]. Other works use compositions of manifold learning models and normalizing flows that are trained simultaneously, e.g., the  $\mathcal{M}$ -Flow [8], Noisy Injective Flows [15], piecewise injective flows called Trumpets [16], and neural manifold ordinary differential equations [17]. Another distinct approach of training normalizing flows on manifold data is by inflation with Gaussian noise to overcome the manifold structure [18].

Opposed to the PCA dimensionality reduction, most injective normalizing flows do not support exact PDF tractability and instead require PDF approximations [8] or approximations of the inverse transformation [15]. Notable exceptions are the conformal embedding flow [19] and the principal manifold flow [20] that maintain tractable PDFs. Most injective normalizing flows are designed to perform manifold learning and density estimation using the same transformation. Hence, likelihood maximization and manifold learning have to be trained either simultaneously [19] or iteratively [8]. This leads to a difficult tuning problem as the loss function has to balance two uneven objectives, namely, the likelihood maximization, which is unbounded [5], and the reconstruction loss of the manifold learning that has a theoretical global optimum of zero.

In this work, we generalize our work on PCA-based dimensionality reduction [10] to nonlinear embeddings by extending our findings to compositions of arbitrary isometric embeddings and normalizing flows. We show theoretically that the PDF described by an injective normalizing flow is invariant to isometric embeddings, in general, rather than just to the PCA, specifically. In analogy to our findings for PCA, the isometry of the embeddings allows us to separate the embedding and the normalizing flow training, which avoids the trade-offs from balancing the two objectives of likelihood maximization and manifold learning. Hence, we can train both model parts to the highest attainable accuracy. Meanwhile, the composition still allows for explicit sampling as well as explicit and efficient PDF computations.

The remainder of this paper is organized as follows: In Section 2, we briefly review the basic principles of normalizing flows, present the general concept of injective normalizing flows, and explicate the difficulties associated with the combination of manifold learning and density estimation. Then, we show theoretically that PDFs described by injective

normalizing flows are invariant to isometric embeddings and review the isometric condition of the PCA and the I-AE. In Section 3, we apply the injective normalizing flows to generate samples of the artificial S-curve data set and the MNIST image data set of handwritten digits. Finally, Section 4 concludes our work.

## 2 Isometric embedding normalizing flows

We first review the basic principles of normalizing flows in Section 2.1. Then, we state the general loss function for an injective normalizing flow with combined manifold learning, in Section 2.2. In Section 2.3, we show theoretically that the change of variables of the PDF is invariant to isometric embeddings, which allows us to separate manifold learning and density estimation into two separate problems. Finally, in Section 2.4 and Section 2.5 we show how PCA and I-AE build affine and nonlinear isometric embeddings for normalizing flows, respectively.

### 2.1 Normalizing flows

Normalizing flows model the probability distribution of a  $D$ -dimensional multivariate random variable  $X$  through a change of variables of a multivariate standard Gaussian [21]. The change of variables utilizes a diffeomorphism, i.e., a bijective and differentiable transformation,  $T(\cdot) : \mathbb{R}^D \rightarrow \mathbb{R}^D$ . Thus, each point in the data probability distribution  $\mathbf{x}$  is uniquely mapped to a point in the Gaussian  $\mathbf{z}$  and vice versa. The links are given by the forward  $T(\cdot)$  and inverse  $T^{-1}(\cdot)$  transformation, respectively. Exploiting the diffeomorphism, the PDF  $p_X(\mathbf{x})$  can be calculated explicitly using the change of variables formula [21]:

$$p_X(\mathbf{x}) = \phi(\mathbf{z}) |\det \mathbf{J}_T(\mathbf{z})|^{-1} \quad (1)$$

Here,  $\mathbf{J}_T$  is the Jacobian of the transformation  $T$  and  $\phi(\mathbf{z})$  is the Gaussian PDF. Given a data set  $\mathcal{X}$  and a trainable diffeomorphism  $T_\theta$  with parameters  $\theta$ , the logarithm of Equation (1) can be used to train the normalizing flow via direct log-likelihood maximization [21].

### 2.2 Injective normalizing flows

Given a  $d$ -dimensional manifold  $\mathcal{M} \subset \mathbb{R}^D$  with  $d < D$ , let  $\psi(\cdot) : \mathbb{R}^d \rightarrow \mathcal{M}$  be a decoder function that

maps the data from the latent space  $\mathbf{z}$  to the data space  $\mathbf{x}$  and let  $\psi^{-1}(\cdot) : \mathbb{R}^D \rightarrow \mathbb{R}^d$  be an encoder function:

$$\begin{aligned}\mathbf{x} &= \psi(\mathbf{z}) \\ \mathbf{z} &= \psi^{-1}(\mathbf{x})\end{aligned}$$

Then,  $\psi^{-1}$  is the pseudo-inverse of  $\psi$ , i.e., an exact inverse of  $\psi$  for  $\mathbf{x} \in \mathcal{M}$ . Since using encoder and decoder functions results in non-square Jacobians, the change of variables has to be set up in a generalized form [13]:

$$p_X(\mathbf{x}) = \phi(\mathbf{z}) |\det(\mathbf{J}_\psi(\mathbf{z})^T \mathbf{J}_\psi(\mathbf{z}))|^{-0.5} \quad (2)$$

If the injective normalizing flow is used for both density estimation and manifold learning, the reconstruction loss has to be considered in addition to the likelihood maximization. The combined loss function then is the expectation of the two parts over the distribution of the random variable  $X$  [8]:

$$\mathcal{L} = \mathbb{E}_X [-\log p_X(\mathbf{x}) + \beta \|\mathbf{x} - \psi(\psi^{-1}(\mathbf{x}))\|_2] \quad (3)$$

In Equation (3),  $\|\cdot\|_2$  is the Euclidean norm and  $\beta$  is a scaling hyperparameter to balance the two loss function components. In general, injective normalizing flows require manifold learning and likelihood maximization to be performed either simultaneously [16, 19] or iteratively [8]. However, this balancing is particularly difficult, as the reconstruction loss  $\|\mathbf{x} - \psi(\psi^{-1}(\mathbf{x}))\|_2$  is bounded from below by zero, while the likelihood loss  $-\log p_X(\mathbf{x})$  is theoretically unbounded. Furthermore, the absolute values of the likelihood vary by orders of magnitude between data sets, which makes tuning the hyperparameter  $\beta$  difficult.

## 2.3 Isometric embeddings

As an alternative to performing both manifold learning and density estimation with a single model, we design the manifold normalizing flow as a composition of an isometric manifold learning model and a normalizing flow model, thereby separating the two objectives. The full transformation  $\psi$  then consists of an injective transformation  $f(\cdot) : \mathbb{R}^d \rightarrow \mathcal{M}$  with pseudo inverse  $g(\cdot) : \mathcal{M} \rightarrow \mathbb{R}^d$  and a diffeomorphism  $T(\cdot) : \mathbb{R}^d \rightarrow \mathbb{R}^d$  in the lower-dimensional latent space:

$$\begin{aligned}\mathbf{x} &= \psi(\mathbf{z}) = f \circ T(\mathbf{z}) \\ \mathbf{z} &= \psi^{-1}(\mathbf{x}) = T^{-1} \circ g(\mathbf{x})\end{aligned}$$

Applying the chain rule of differentiation to Equation (2), the change of variables of the composition is given by [8]:

$$p_X(\mathbf{x}) = \phi(\mathbf{z}) |\det \mathbf{J}_T(\mathbf{z})|^{-1} \left| \det \left( \mathbf{J}_f(T(\mathbf{z}))^T \mathbf{J}_f(T(\mathbf{z})) \right) \right|^{-0.5} \quad (4)$$

Here, the term  $\det \left( \mathbf{J}_f(T(\mathbf{z}))^T \mathbf{J}_f(T(\mathbf{z})) \right)$  is typically very expensive to compute. Options on how to mitigate the computational cost are using approximate Jacobian determinants [8], identifying the Riemannian metric [22, 23], or learning embeddings of Riemannian manifolds directly [17]. In our previous work [10], we highlighted that the Jacobian determinant of the embedding is always equal to one if the encoding is performed via PCA, i.e., the PDF in Equation (4) is invariant to a PCA encoding. In the following, we extend this finding to isometric embeddings, in general.

The Nash embedding theorem [24] states that isometric embeddings can encode  $d$ -dimensional manifolds embedded in  $D$ -dimensional ambient space arbitrarily well if  $D \geq d + 1$ , i.e., we can require the decoder  $f$  to be isometric and the encoder  $g$  to be a pseudo-inverse of  $f$  without a loss of information in the embedding. Isometric transformations, in general, are defined as distance preserving transformations. Mathematically, this can be expressed as

$$\mathbf{J}_f(\mathbf{z})^T \mathbf{J}_f(\mathbf{z}) = \mathbf{I}_d \quad \forall \mathbf{z} \in \mathbb{R}^d,$$

where  $\mathbf{I}_d$  is the  $d$ -dimensional identity matrix. As the determinant of the identity matrix is one, the PDF in Equation (4) is invariant to the isometric embedding. Therefore, the likelihood function for any isometric embedding can be simplified to:

$$p_X(\mathbf{x}) = \phi(\mathbf{z}) |\det \mathbf{J}_T(\mathbf{z})|^{-1} \quad (5)$$

A visual representation of the two-step composition is shown in Figure 1.

In conclusion, the PDF of an injective normalizing flow is invariant to isometric embedding functions. Therefore, the isometric embedding can be trained independently from the normalizing flow without the need for any adjustments to the normalizing flow training. This avoids the need to balance the two objectives of likelihood-maximization and reconstruction loss described in Equation (3) and allows us to train both models to high accuracy.

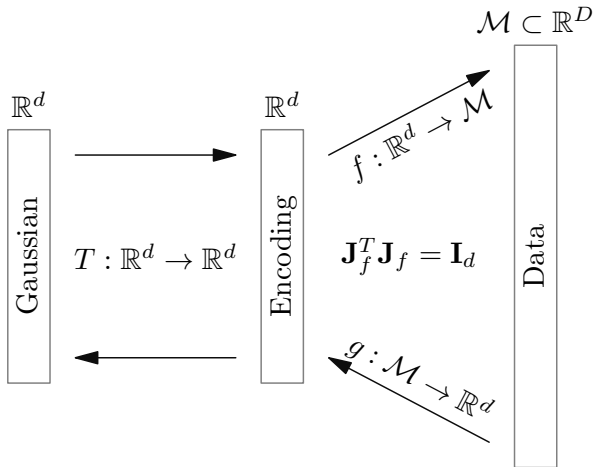


**Fig. 1.** Injective normalizing flow designed as a composition of a diffeomorphism  $T : \mathbb{R}^d \rightarrow \mathbb{R}^d$  and an isometric embedding  $f : \mathbb{R}^d \rightarrow \mathcal{M}$  with pseudo inverse  $g : \mathcal{M} \rightarrow \mathbb{R}^d$ .

## 2.4 Affine isometric embedding with PCA

For completeness, this section reviews the use of PCA as affine isometric embedding for normalizing flows from our previous work [10]. For PCA, both the encoder  $g_{\text{PCA}}$  and the decoder  $f_{\text{PCA}}$  are affine transformations [25]:

$$\begin{aligned} \mathbf{x} &= f_{\text{PCA}}(\mathbf{z}) = \mathbf{V}_d \mathbf{z} + \boldsymbol{\mu}_{\mathcal{X}} \\ \mathbf{z} &= g_{\text{PCA}}(\mathbf{x}) = \mathbf{V}_d^T (\mathbf{x} - \boldsymbol{\mu}_{\mathcal{X}}) \end{aligned}$$

Here,  $\boldsymbol{\mu}_{\mathcal{X}}$  is the empirical mean of the dataset  $\mathcal{X}$  and  $\mathbf{V}_d \in \mathbb{R}^{D \times d}$  are the first  $d$  column vectors of the matrix of right singular vectors  $\mathbf{V} \in \mathbb{R}^{D \times D}$  that stems from the singular value decomposition (SVD) of the empirical covariance matrix  $\mathbf{K}_{\mathcal{X}, \mathcal{X}} \in \mathbb{R}^{D \times D}$ :

$$\mathbf{K}_{\mathcal{X}, \mathcal{X}} = \frac{1}{N-1} \sum_{i=1}^N (\mathbf{x}_i - \boldsymbol{\mu}_{\mathcal{X}})(\mathbf{x}_i - \boldsymbol{\mu}_{\mathcal{X}})^T = \mathbf{U} \boldsymbol{\Sigma} \mathbf{V}^T \quad (6)$$

In Equation (6),  $\mathbf{U} \in \mathbb{R}^{D \times D}$  is the matrix of left singular vectors and  $\boldsymbol{\Sigma} \in \mathbb{R}^{N \times N}$  is a diagonal matrix with the singular values on its diagonal. Because PCA is an affine transformation,  $\mathbf{V}_d$  is the constant Jacobian of the decoding transformation  $f_{\text{PCA}}$ , hence:  $\mathbf{J}_{f_{\text{PCA}}} = \mathbf{V}_d = \text{const.}$  By design of the SVD,  $\mathbf{V}_d$  has orthonormal column vectors and thus:

$$\mathbf{J}_{f_{\text{PCA}}}^T \mathbf{J}_{f_{\text{PCA}}} = \mathbf{V}_d^T \mathbf{V}_d = \mathbf{I}_d$$

For PCA, the latent dimensionality  $d$  is equal to the number of considered principal components. We

base the selection of  $d$  on the explained variance ratio, i.e., the singular values  $\sigma_k$  of the empirical covariance matrix  $\mathbf{K}_{\mathcal{X}, \mathcal{X}}$  normalized by their total sum. The sum over the explained variance ratio of the considered principal components then is the cumulative explained variance (CEV):

$$\text{CEV} = \frac{\sum_{k=1}^d \sigma_k}{\sum_{i=1}^D \sigma_i} 100\%$$

In practice, we select  $d$  such that the CEV is greater or equal to the desired percentage, e.g., 99%.

## 2.5 Nonlinear isometric embeddings with I-AE

As a nonlinear isometric embedding, we utilize the isometric autoencoder (I-AE) proposed by Gropp et al. [26]. The I-AE uses a nonlinear autoencoder and specifically enforces the isometry during training via penalization. Both encoder  $g_{\text{I-AE}}$  and decoder  $f_{\text{I-AE}}$  are deep neural networks  $\mathbf{G}(\mathbf{x}; \boldsymbol{\theta}_{\mathbf{G}})$  and  $\mathbf{F}(\mathbf{z}; \boldsymbol{\theta}_{\mathbf{F}})$ , respectively:

$$\begin{aligned} \mathbf{x} &= f_{\text{I-AE}}(\mathbf{z}) = \mathbf{F}(\mathbf{z}; \boldsymbol{\theta}_{\mathbf{F}}) \\ \mathbf{z} &= g_{\text{I-AE}}(\mathbf{x}) = \mathbf{G}(\mathbf{x}; \boldsymbol{\theta}_{\mathbf{G}}) \end{aligned}$$

Here,  $\boldsymbol{\theta}_{\mathbf{F}}$  and  $\boldsymbol{\theta}_{\mathbf{G}}$  are the parameters of decoder and encoder, respectively. To minimize the loss of information, the loss function penalizes the mean-squared-error in the reconstruction:

$$\mathcal{L}_{\text{AE}}(\boldsymbol{\theta}_{\mathbf{G}}, \boldsymbol{\theta}_{\mathbf{F}}) = \mathbb{E}_{\mathcal{X}} \{ \|\mathbf{x} - \mathbf{F}(\mathbf{G}(\mathbf{x}))\|_2 \} \quad (7)$$

Furthermore, the training has to promote the isometry of the decoder:

$$\mathbf{J}_{\mathbf{F}}(\mathbf{z})^T \mathbf{J}_{\mathbf{F}}(\mathbf{z}) = \mathbf{I}_d \quad \forall \mathbf{z} \in \mathbb{R}^d \quad (8)$$

Computing the expression in Equation (8), however, requires expensive matrix multiplications of the Jacobian and its transpose. To avoid these, Gropp et al. [26] propose enforcing the isometry condition implicitly by penalizing the change in length of a vector to the surface of the unit ball  $\mathbf{u} \in \mathbb{S}^{d-1} = \{\mathbf{y} \in \mathbb{R}^d : \|\mathbf{y}\|_2 = 1\}$ , i.e., a unit vector, after multiplication with the Jacobian:

$$\mathcal{L}_{\text{iso}}(\boldsymbol{\theta}_{\mathbf{F}}) = \mathbb{E}_{\mathcal{Z}, \mathbf{U}} \left\{ \left( \|\mathbf{J}_{\mathbf{F}}(\mathbf{z}) \mathbf{u}\|_2 - 1 \right)^2 \right\} \quad (9)$$

Here,  $\mathbb{E}_{\mathcal{Z}, \mathbf{U}}$  is the expectation over the latent space  $\mathbf{z} \in \mathbb{R}^d$  and the space of all unit vectors  $\mathbf{u} \in \mathbb{S}^{d-1}$ . In addition to the isometry loss of the decoder, the isometry of the encoder (pseudo inverse) has to be promoted as well:

$$\mathcal{L}_{\text{piso}}(\boldsymbol{\theta}_{\mathbf{G}}) = \mathbb{E}_{\mathcal{X}, \mathbf{U}} \left\{ \left( \|\mathbf{u}^T \mathbf{J}_{\mathbf{G}}(\mathbf{x})\|_2 - 1 \right)^2 \right\} \quad (10)$$

Here,  $\mathbb{E}_{X,U}$  is the expectation over the manifold  $\mathbf{x} \in \mathcal{M}$  and the space of all unit vectors  $\mathbf{u} \in \mathbb{S}^{d-1}$ . Finally, the three loss functions are combined to a total loss using weights  $\lambda_{\text{iso}}$  and  $\lambda_{\text{piso}}$  for  $\mathcal{L}_{\text{iso}}$  and  $\mathcal{L}_{\text{piso}}$ , respectively:

$$\begin{aligned} \mathcal{L}(\boldsymbol{\theta}_{\mathbf{G}}, \boldsymbol{\theta}_{\mathbf{F}}) = & \mathcal{L}_{\text{AE}}(\boldsymbol{\theta}_{\mathbf{G}}, \boldsymbol{\theta}_{\mathbf{F}}) \\ & + \lambda_{\text{iso}} \mathcal{L}_{\text{iso}}(\boldsymbol{\theta}_{\mathbf{F}}) + \lambda_{\text{piso}} \mathcal{L}_{\text{piso}}(\boldsymbol{\theta}_{\mathbf{G}}) \end{aligned} \quad (11)$$

Unlike PCA, the I-AE does not come with a recipe to estimate the latent dimensionality  $d$ , i.e.,  $d$  must be determined via empirical studies [26]. For more details on the implementation, selection of the weights  $\lambda_{\text{iso}}$  and  $\lambda_{\text{piso}}$ , and the computation of the loss functions, we refer to the original I-AE publication [26].

### 3 Numerical experiments

We apply the proposed combination of isometric embeddings and normalizing flows to learn and sample from the probability distributions of multiple different data sets. Specifically, we analyze the generated samples from both standard full-space normalizing flows and isometric embedding flows in comparison to the real data. The two data sets are the synthetic S-Curve data set provided by the machine learning library scikit-learn [27] and the MNIST data set with images of handwritten digits [28]. For all normalizing flow models, we employ the RealNVP affine coupling layer architecture [6] as the invertible neural network. All models are implemented in TensorFlow, version 2.5.0 [29].

#### 3.1 S-Curve

The S-Curve data set describes a two-dimensional, nonlinear manifold embedded in three-dimensional Euclidean space (see left of Figure 2). We omit an application of PCA due to the nonlinear nature of the S-Curve. Following the training methodology derived in Section 2, we first train the I-AE using Equation (11) and then train a two-dimensional RealNVP model. Figure 2 shows the reconstruction (center) and the latent space (right) of the trained I-AE for a test set  $\mathcal{X}_{\text{test}}$  of 1000 samples. The results in Figure 2 clearly show that the encoding leads to an unfolding of the three-dimensional S-shape to a two-dimensional rectangle and that the full S-Curve is recovered by the decoder. Table 1 shows the final training and test losses for the total and the three constituents of the loss function. To verify that the embedding is in fact isometric, we compute the Jacobian determinant of the decoder. For



**Fig. 2.** Encoding and decoding of three-dimensional S-Curve data (1000 samples) [27] using I-AE [26]. Test data  $\mathbf{x} \in \mathcal{X}_{\text{test}}$  (left); reconstruction of test data  $f(g(\mathbf{x})) \forall \mathbf{x} \in \mathcal{X}_{\text{test}}$  (center); two-dimensional latent space of I-AE  $g(\mathbf{x}) \forall \mathbf{x} \in \mathcal{X}_{\text{test}}$  (right). Colorcoding is based on position of test data.

**Tab. 1.** Final training loss and test loss for I-AE training on the S-Curve data set [27]. The constituents of the loss function are defined in Equations (11), (7), (9), and (10).

	$\mathcal{L}$	$\mathcal{L}_{\text{AE}}$	$\mathcal{L}_{\text{iso}}$	$\mathcal{L}_{\text{piso}}$
Training	$2.21 \times 10^{-4}$	$1.55 \times 10^{-4}$	$4.78 \times 10^{-5}$	$1.87 \times 10^{-5}$
Test	$2.11 \times 10^{-4}$	$1.54 \times 10^{-4}$	$3.81 \times 10^{-5}$	$1.89 \times 10^{-5}$

the 1000-sample test set  $\mathcal{X}_{\text{test}}$ , the expectation of the Jacobian determinant is:

$$\mathbb{E}_{\mathcal{X}_{\text{test}}} \left\{ \left| \det \mathbf{J}_{\mathbf{F}}(\mathbf{G}(\mathbf{x}))^T \mathbf{J}_{\mathbf{G}}(\mathbf{x}) \right|^{-0.5} \right\} = 1.0096$$

Thus, the PDF in Equation (5) only deviates by a factor of 1.0096 from an exact isometry.

Figure 3 shows sampled data of the normalizing flow with I-AE embedding (center) in comparison to a full-space normalizing flow (right). The results show that the manifold shape is correctly recovered by the injective flow, whereas the full-space normalizing flow fails to reconstruct the shape of the S-Curve distribution. Note that we do not show the absolute PDF values of the injective (Equation (5)) and full space normalizing flow (Equation (1)), as they describe the PDFs of two systems with differ-



**Fig. 3.** 1000 generated S-Curve samples [27]. Test data  $\mathbf{x} \in \mathcal{X}_{\text{test}}$  (left); samples from RealNVP in reduced space with I-AE embedding (center); samples from RealNVP in full space (right). The colors are based on the z-axis of the respective data points.

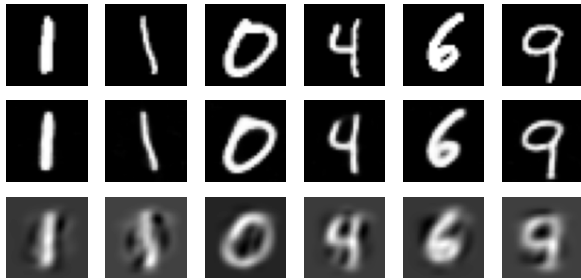


**Fig. 4.** I-AE and PCA reconstruction after encoding of MNIST data set of handwritten digits [28]. Row 1: Samples from the test set, row 2: Reconstruction after encoding with I-AE, row 3: Reconstruction after encoding with PCA. Latent dimensionalities for I-AE and PCA are 16 based on original I-AE paper [26].

**Tab. 2.** Reconstruction loss of PCA and I-AE for MNIST test data set [28]. The table shows the mean-squared-error (MSE) and the mean-absolute-error (MAE) with data scaled to  $[0, 1]$ .

	I-AE	PCA
MSE	$8.28 \times 10^{-3}$	$2.69 \times 10^{-2}$
MAE	$3.20 \times 10^{-2}$	$8.81 \times 10^{-2}$

ent dimensionality and are, therefore, not comparable.

The results in Figure 2 and Table 1 show that the I-AE learns embeddings with very high accuracy. Furthermore, the learned embedding is almost isometric, which justifies its usage in an injective normalizing flow as proposed in Section 2. This finding is confirmed by the generated data from the combination of I-AE and RealNVP, which reconstructs the true distribution with only a few outliers.

### 3.2 MNIST

Finally, we consider the MNIST data set of handwritten digits [28] with  $28 \times 28$  pixel resolution. For both the I-AE and PCA, we use latent dimensionalities of 16 based on the original I-AE paper [26]. Figure 4 shows a random selection of images from the MNIST test set (first row) as well as the reconstruction of these images after encoding using I-AE (second row) and PCA (third row), respectively. For all test images in Figure 4, the I-AE is able to preserve the images well. The PCA reconstruction shows a loss of features, blurred digits, and a significant amount of noise around the digits. In addition to the visual comparison in Fig-

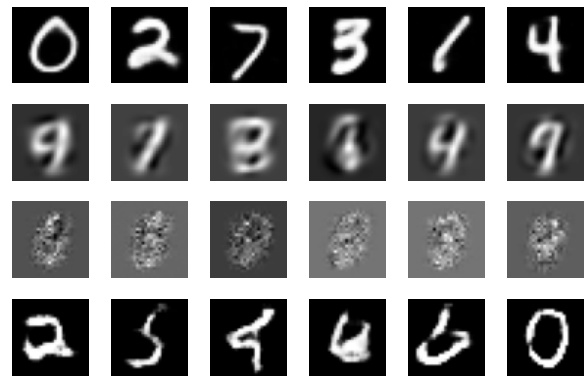


**Fig. 5.** Generated images of MNIST data set of handwritten digits [28]. Row 1: Random samples of the I-AE and RealNVP composition, row 2: Random samples of the PCA and RealNVP composition, row 3: random samples from a full-space RealNVP, row 4: random samples from a Wasserstein GAN [30]. Latent dimensionalities for I-AE and PCA are 16.

ure 4, Table 2 lists the mean-squared-error (MSE) and mean-absolute-error (MAE) for both PCA and I-AE on the MNIST test set. With respect to both metrics, the I-AE achieves lower values compared to the PCA. In conclusion, the nonlinear I-AE shows a better ability to encode the data compared to the affine PCA, which indicates that the MNIST data set is embedded on a nonlinear manifold.

Next, we train different RealNVP models on samples encoded using I-AE and PCA as well as the full images. Figure 5 shows samples from the combined isometric embedding normalizing flows in comparison to a full  $28 \times 28$ -dimensional normalizing flow. For reference, we also include images generated using a Wasserstein-GAN (W-GAN) [30], which is often the method of choice for image generation [1]. Note that the W-GAN was significantly more difficult to train and fine-tune compared to the isometric embedding normalizing flows. Hence, the presented W-GAN results are the best of 20 trained models. Meanwhile, both isometric normalizing flow compositions converge to the same result in almost every iteration.

The generated images from the composition of I-AE and RealNVP (row 1) appear like handwritten digits from the original MNIST data set. The images generated from the RealNVP with PCA embedding (row 2) resemble handwritten digits to some extent. However, as observed in Figure 4 the images are blurred, and the digits are difficult to read or ambiguous. The full-space normalizing

**Tab. 3.** Inception score (IS) [31] and Fréchet inception distance (FID) [32] for MNIST test set  $\mathcal{X}_{\text{Test}}$  and generated images from I-AE and PCA compositions with RealNVP, full-space RealNVP (FSNF), and Wasserstein-GAN (W-GAN). The number of generated images is 50000, and the mean and standard deviation for the IS are computed over 10 batches. A high IS and low FID indicate good scores.

	IS	FID
$\mathcal{X}_{\text{Test}}$	$11.39 \pm 0.39$	-
I-AE	$12.10 \pm 0.35$	46.60
PCA	$7.04 \pm 0.25$	724.51
FSNF	$2.55 \pm 0.08$	1011.60
W-GAN	$12.15 \pm 0.51$	95.10

flow-generated images (row 3) are very noisy and do not resemble handwritten digits at all, i.e., the full-space RealNVP was unable to learn the probability distribution of the MNIST data set. The W-GAN generated images (row 4) show lines with high contrast that resemble digits to some extent. However, these digits are often incomplete or ambiguous. Apparently, the discriminator model fails to identify at least some of the images in row 4 as fake.

In addition to the visual analysis (cf. Figure 5), we compute the inception score (IS) [31] and the Fréchet inception distance (FID) [32] for each variant of the normalizing flow and the W-GAN. Both IS and FID are quantitative measures that analyze both the quality as well as the diversity of the generated images. While the IS considers generated samples only, the FID also includes information from the real data. In general, the IS is a positively oriented score, i.e., high scores indicate high-quality data sets, and the FID is a negatively oriented score. We use a classifier model with  $>99.3\%$  accuracy. As recommended by Salimans et al. [31], we generated 50000 samples from each normalizing flow variant to compute both IS and FID. For the IS, we batch the data set and compute the empirical mean and standard deviation. Table 3 lists IS and FID for the generated image data sets.

The results in Table 3 highlight that the image data set generated using the I-AE embedding scores as high as the test set with real images with respect to the IS and also shows the lowest FID of all models. The W-GAN scores an IS as good as the I-AE but shows a higher FID than the I-AE. The results suggest that the W-GAN images are diverse and can be classified well as indicated by the IS,

but do not resemble the actual data as well as the I-AE normalizing flow as highlighted by the FID. The IS also correctly indicates a lower quality of the images generated using the PCA embedding as well as the exceptionally low quality of the FSNF-generated images. Thus, the quantitative results in Table 3 confirm our conclusions from the visual assessment in Figure 5.

In conclusion, the isometric dimensionality reduction vastly increases the quality of the generated images and outperforms the W-GAN reference. In fact, the I-AE learns highly accurate encodings of the MNIST data set despite a latent dimensionality as low as 16. Our analysis of Figure 5 and Table 3, thus, shows that the composition of I-AE with RealNVP can build highly descriptive and accurate generative models for data that resides on nonlinear manifolds. As expected, the affine PCA shows a distinctively lower quality, which, however, are still far better than the full-space normalizing flow images, which are completely unusable.

## 4 Conclusion

Standard normalizing flows are ill-posed to model manifold distributions and tend to sample unrealistic and out-of-distribution data. To address the challenges of manifold probability distributions, we generalize the PCA dimensionality reduction of our precious work [10] by proposing a two-parted approach that separates injective normalizing flows into an isometric manifold-learning part and a lower-dimensional density estimation part. We show that by definition, the probability density function (PDF) described by the change of variables formula is invariant to isometries. This insight yields two major benefits for the training of the isometric normalizing flow: First, no expensive Jacobian determinant computations result from the embedding. Second, embedding functions and normalizing flow models can be trained sequentially, which avoids difficult balancing of the unbounded likelihood maximization and the bounded reconstruction loss. Therefore, both model parts can be trained to the highest attainable accuracy. After training both parts of the model, the combined approach allows for efficient and explicit sampling as well as PDF evaluations. As PCA is limited to affine embeddings, we utilize the isometric autoencoder (I-AE) [26] as a nonlinear isometric dimensionality reduction scheme that comes with an explicit pseudo-inverse and allows us to build the encoder and decoder models using deep learning architectures like

convolutions and nonlinear activation functions.

In our numerical analysis, we apply the isometric embeddings to the artificial S-Curve dataset and the MNIST dataset of images of handwritten digits. Both PCA and I-AE-based embeddings lead to a better approximation of the true probability distributions and more realistic samples compared to the standard full-space normalizing flow. The I-AE excels in describing the two nonlinear manifolds, S-Curve and MNIST. Moreover, the MNIST samples generated from the composition of I-AE and RealNVP yield synthetic hand-written digits that are indistinguishable from real images, as also evidenced by high inception scores and low Fréchet inception distances.

In conclusion, the proposed combination of isometric embeddings and normalizing flows presents an effective approach to handle manifold data and take full advantage of the benefit from the direct log-likelihood maximization and explicit sampling of normalizing flows. We argue that the separation of embedding and density estimation is of great benefit as both model parts can be trained to high accuracy without trade-offs. Furthermore, the method is easy to implement and train, as it relies on building blocks of well-established methods with open-source implementations.

## Nomenclature

Description	Symbol
Latent dimension	$d$
Data dimensionality	$D$
Decoder	$\mathbf{f}(\mathbf{z})$
Encoder	$\mathbf{g}(\mathbf{x})$
Jacobian	$\mathbf{J}$
Sample covariance of $\mathcal{X}$	$\mathbf{K}_{\mathcal{X},\mathcal{X}}$
Data manifold	$\mathcal{M} \subset \mathbb{R}^D$
Probability density function	$p_{\mathcal{X}}(\mathbf{x})$
Surface of $d$ -dimensional unit ball	$\mathbb{S}^{d-1}$
Diffeomorphism	$T(\cdot)$
Samples of multivariate random variables	$\mathbf{x}, \mathbf{z}$
Random variable	$X$
Data set	$\mathcal{X}$
Sample mean vector of $\mathcal{X}$	$\boldsymbol{\mu}_{\mathcal{X}}$
PDF of standard Gaussian	$\phi(\mathbf{z})$
Parameter vector	$\boldsymbol{\theta}$

## Acknowledgements

This work was performed as part of the Helmholtz School for Data Science in Life, Earth and En-

ergy (HDS-LEE) and received funding from the Helmholtz Association of German Research Centres. This publication is based upon work supported by the King Abdullah University of Science and Technology (KAUST) Office of Sponsored Research (OSR) under Award No. OSR-2019-CRG8-4033, and the Alexander von Humboldt Foundation.

## Bibliography

- [1] Sam Bond-Taylor, Adam Leach, Yang Long, and Chris G Willcocks. Deep generative modelling: A comparative review of VAEs, GANs, normalizing flows, energy-based and autoregressive models, 2021.
- [2] Diederik P Kingma and Max Welling. Auto-encoding variational bayes. *arXiv preprint arXiv:1312.6114*, 2014.
- [3] Ian Goodfellow, Jean Pouget-Abadie, Mehdi Mirza, Bing Xu, David Warde-Farley, Sherjil Ozair, Aaron Courville, and Yoshua Bengio. Generative adversarial nets. In *Advances in Neural Information Processing Systems*, pages 2672–2680. MIT Press, Cambridge, MA, USA, 2014.
- [4] Martin Arjovsky and Léon Bottou. Towards principled methods for training generative adversarial networks, 2017.
- [5] Richard J Rossi. *Mathematical statistics: An introduction to likelihood based inference*. John Wiley & Sons, 2018.
- [6] Laurent Dinh, Jascha Sohl-Dickstein, and Samy Bengio. Density estimation using Real NVP. *arXiv preprint arXiv:1605.08803*, 2017.
- [7] George Papamakarios, Eric Nalisnick, Danilo Jimenez Rezende, Shakir Mohamed, and Balaji Lakshminarayanan. Normalizing flows for probabilistic modeling and inference. *arXiv preprint arXiv:1912.02762*, 2019.
- [8] Johann Brehmer and Kyle Cranmer. Flows for simultaneous manifold learning and density estimation. *arXiv preprint arXiv:2003.13913*, 2020.
- [9] Jens Behrmann, Paul Vicol, Kuan-Chieh Wang, Roger Grosse, and Joern-Henrik Jacobsen. Understanding and mitigating exploding inverses in invertible neural networks.

- In Arindam Banerjee and Kenji Fukumizu, editors, *Proceedings of The 24th International Conference on Artificial Intelligence and Statistics*, volume 130 of *Proceedings of Machine Learning Research*, pages 1792–1800. PMLR, 13–15 Apr 2021.
- [10] Eike Cramer, Alexander Mitsos, Raúl Tempone, and Manuel Dahmen. Principal component density estimation for scenario generation using normalizing flows. *arXiv preprint arXiv:2104.10410*, 2021.
- [11] Charles Fefferman, Sanjoy Mitter, and Hariharan Narayanan. Testing the manifold hypothesis. *Journal of the American Mathematical Society*, 29(4):983–1049, 2016.
- [12] Madeleine Udell and Alex Townsend. Why are big data matrices approximately low rank? *SIAM Journal on Mathematics of Data Science*, 1(1):144–160, 2019.
- [13] Mevlana C. Gemici, Danilo Rezende, and Shakir Mohamed. Normalizing flows on Riemannian manifolds. *arXiv preprint arXiv:1611.02304*, 2016.
- [14] Danilo Jimenez Rezende, George Papamakarios, Sébastien Racaniere, Michael Albergo, Gurtej Kanwar, Phiala Shanahan, and Kyle Cranmer. Normalizing flows on tori and spheres. In *International Conference on Machine Learning*, pages 8083–8092. PMLR, 2020.
- [15] Edmond Cunningham, Renos Zabounidis, Abhinav Agrawal, Ina Fiterau, and Daniel Sheldon. Normalizing flows across dimensions. *arXiv preprint arXiv:2006.13070*, 2020.
- [16] Konik Kothari, AmirEhsan Khorashadizadeh, Maarten de Hoop, and Ivan Dokmanić. Trumpets: Injective flows for inference and inverse problems. *arXiv preprint arXiv:2102.10461*, 2021.
- [17] Aaron Lou, Derek Lim, Isay Katsman, Leo Huang, Qingxuan Jiang, Ser-Nam Lim, and Christopher De Sa. Neural manifold ordinary differential equations. *arXiv preprint arXiv:2006.10254*, 2020.
- [18] Christian Horvat. Density estimation on low-dimensional manifolds: an inflation-deflation approach. *arXiv preprint arXiv:2105.12152*, 2021.
- [19] Brendan Leigh Ross and Jesse C Cresswell. Conformal embedding flows: Tractable density estimation on learned manifolds. In *ICML Workshop on Invertible Neural Networks, Normalizing Flows, and Explicit Likelihood Models*, pages 1–11. ICML, 2021.
- [20] Edmond Cunningham, Adam Cobb, and Susmit Jha. Principal manifold flows. *arXiv preprint arXiv:2202.07037*, 2022.
- [21] George Papamakarios, Eric Nalisnick, Danilo Jimenez Rezende, Shakir Mohamed, and Balaji Lakshminarayanan. Normalizing flows for probabilistic modeling and inference. *Journal of Machine Learning Research*, 22(57):1–64, 2021.
- [22] Dominique Perraul-Joncas and Marina Meilã. Non-linear dimensionality reduction: Riemannian metric estimation and the problem of geometric discovery. *arXiv preprint arXiv:1305.7255*, 2013.
- [23] James McQueen, Marina Meilã, Jacob VanderPlas, and Zhongyue Zhang. Megaman: scalable manifold learning in python. *The Journal of Machine Learning Research*, 17(1):5176–5180, 2016.
- [24] John Nash. The imbedding problem for Riemannian manifolds. *Annals of Mathematics*, pages 20–63, 1956.
- [25] Karl Pearson. On lines and planes of closest fit to systems of points in space. *The London, Edinburgh, and Dublin Philosophical Magazine and Journal of Science*, 2(11):559–572, 1901.
- [26] Amos Gropp, Matan Atzmon, and Yaron Lipman. Isometric autoencoders. *arXiv preprint arXiv:2006.09289*, 2020.
- [27] F. Pedregosa, G. Varoquaux, A. Gramfort, V. Michel, B. Thirion, O. Grisel, M. Blondel, P. Prettenhofer, R. Weiss, V. Dubourg, J. Vanderplas, A. Passos, D. Cournapeau, M. Brucher, M. Perrot, and E. Duchesnay. Scikit-learn: Machine learning in Python. *Journal of Machine Learning Research*, 12:2825–2830, 2011.
- [28] Yann LeCun and Corinna Cortes. MNIST handwritten digit database, 2010. <http://yann.lecun.com/exdb/mnist/>, accessed on 10-10-2021.

- 
- [29] Martín Abadi and Ashish Agarwal. TensorFlow: Large-scale machine learning on heterogeneous systems, 2015. Software available from tensorflow.org, accessed on 08-08-2021.
- [30] Martin Arjovsky, Soumith Chintala, and Léon Bottou. Wasserstein GAN. *arXiv preprint arXiv:1701.07875*, 2017.
- [31] Tim Salimans, Ian Goodfellow, Wojciech Zaremba, Vicki Cheung, Alec Radford, and Xi Chen. Improved techniques for training GANs. In *Proceedings of the 30th International Conference on Neural Information Processing Systems*, pages 2234–2242. Curran Associates Inc., Red Hook, NY, USA, 2016.
- [32] Martin Heusel, Hubert Ramsauer, Thomas Unterthiner, Bernhard Nessler, and Sepp Hochreiter. GANs trained by a two time-scale update rule converge to a local nash equilibrium. *arXiv preprint arXiv:1706.08500*, 2018.